

Published in final edited form as:

*Phys Rev Appl.* 2020 November 16; 14(5): . doi:10.1103/PhysRevApplied.14.054036.

## Sequential Bayesian experiment design for optically detected magnetic resonance of nitrogen-vacancy centers

Sergey Dushenko<sup>1,2</sup>, Kapildeb Ambal<sup>1,2,3</sup>, Robert D. McMichael<sup>1</sup>

<sup>1</sup>Physical Measurement Laboratory, National Institute of Standards and Technology, Gaithersburg, MD 20899, USA

<sup>2</sup>Institute for Research in Electronics and Applied Physics, University of Maryland, College Park, MD 20742, USA

<sup>3</sup>Department of Physics, Wichita State University, Wichita, KS 67260, USA

### Abstract

In magnetometry using optically detected magnetic resonance of nitrogen vacancy ( $NV^-$ ) centers, we demonstrate more than one order-of-magnitude speed up with sequential Bayesian experiment design as compared with conventional frequency-swept measurements. The  $NV^-$  center is an excellent platform for magnetometry with potential spatial resolution down to few nanometers and demonstrated single-defect sensitivity down to  $nT/Hz^{1/2}$ . The  $NV^-$  center is a quantum defect with spin  $S=1$  and coherence time up to several milliseconds at room temperature. Zeeman splitting of the  $NV^-$  energy levels allows detection of the magnetic field via photoluminescence. We compare conventional  $NV^-$  center photoluminescence measurements that use pre-determined sweeps of the microwave frequency with measurements using a Bayesian inference methodology. In sequential Bayesian experiment design, the settings with maximum utility are chosen for each measurement in real time based on the accumulated experimental data. Using this method, we observe an order of magnitude decrease in the  $NV^-$  magnetometry measurement time necessary to achieve a set precision.

### INTRODUCTION

This study focuses on magnetometry using optically detected magnetic resonance of  $NV^-$  centers. The ability to optically prepare and manipulate spin states, along with a long spin lifetime and robustness to the environment made  $NV^-$  centers a promising platform for application in various areas. A few prominent examples include quantum computing [1], cryptography [2] and memory [3,4]; bio-compatible markers [5] and drug delivery [6]; mechanical [7], temperature [8,9], electric [10] and magnetic sensors [11–13]. The concept of  $NV^-$  center magnetometry [14] was experimentally demonstrated in 2008 in two independent studies by Balasubramanian *et al.* [11] and Maze *et al.* [12], followed by hundreds of other studies [15].

Magnetometry-based imaging using  $NV^-$  centers promises several advantages over the existing magnetic imaging and scanning techniques. The  $NV^-$  center does not carry a significant magnetic moment, making it a non-invasive technique, unlike magnetic force microscopy (MFM) which can suffer from the interaction between sample and the magnetic

tip. Magneto-optic Kerr effect (MOKE) microscopy is limited by optical resolution and is mostly suitable only for studying materials with a strong Kerr effect. In contrast, NV<sup>-</sup> center magnetometry spatial resolution is ultimately only limited by the distance between NV<sup>-</sup> center and the sample, which can be less than ten nanometers [16]. Superconducting quantum interference device (SQUID) magnetometry provides unrivaled sensitivity but requires cryogenic temperatures, and has low spatial resolution, though attempts at miniaturizing the technology are in progress [17]. NV<sup>-</sup> center magnetometry can operate in a broad range of temperatures, including room temperature and above. These advantages make NV<sup>-</sup> center an excellent platform for magnetometry [15,18,19] with potential spatial resolution down to few nanometers and demonstrated sensitivity down to nT/Hz<sup>1/2</sup> [20,21].

Recent research efforts have been directed at increasing the speed and precision of NV<sup>-</sup> center magnetometry measurements. Some of these research efforts summon help from additional hardware to achieve the goal. By modulating the microwave frequency that drives spin-state transitions of the NV<sup>-</sup> center and by demodulating the photoluminescence signal using lock-in amplifiers, significant gains in signal-to-noise ratio and measurement speed have been achieved [20,22–24]. However, such an approach generally requires a high photoluminescence signal by simultaneous measurement of multiple NV<sup>-</sup> centers, which sacrifices the spatial resolution. Another approach that uses specialized hardware is using the differential photon rate meter that can track photoluminescence signal even at low photon count rate, though it does not significantly improve signal-to-noise ratio [25]. In addition to “hardware” approaches, sophisticated algorithms—“software” approaches—have also shown promise. Simulations have showed that neural networks improve NV<sup>-</sup> center readout fidelity [26]. Sequential Bayesian experiment design [27] is another promising machine learning “software” approach. Theoretical studies have discussed how Bayesian methodology [28–31] can be used in determining the unknown parameters of a quantum system [32–36], and magnetometry in particular [37–40]. Encouragingly, in recent experimental studies Bayesian methodology has proven to be advantageous in quantum Hamiltonian learning [41] and measurements of pulsed Ramsey magnetometry using NV<sup>-</sup> centers [42,43]. In this study, we show how combining sequential Bayesian experiment design with conventional optically detected magnetic resonance NV<sup>-</sup> center magnetometry leads to better measurement strategies. In particular, we carry out experiments that compare using a conventional—swept-frequency NV<sup>-</sup> center magnetometry protocol—with the measurements that incorporate sequential Bayesian experiment design.

## BACKGROUND

Many of the useful properties of NV<sup>-</sup> centers hinge on the fact that their photoluminescence depends on their spin state. The NV<sup>-</sup> center is created when two adjacent carbon atoms in a diamond lattice are substituted with a vacancy and a negatively charged nitrogen atom, forming a spin  $S = 1$  quantum defect (Fig. 1(a), see Supplemental Material [44] section S.1 for more details). Photon absorption moves the NV<sup>-</sup> center from the ground state to the excited state, while preserving its spin projection  $m_S$  (Fig. 1(b)) [45,46]. Eventually, the center relaxes back to the ground state, but the relaxation process is spin dependent. An excited state with  $m_S = 0$  mostly relaxes back to the ground state with  $m_S = 0$  by emitting a red photon. In contrast, the excited state with  $m_S = \pm 1$ , can relax by two mechanisms: either

back to the ground state with  $m_S = \pm 1$  by emitting a red photon, or to any  $m_S$  through a dark state, without emitting a visible photon (detailed energy level structure of  $NV^-$  center can be found in Supplemental Material S.1). Hence, photoluminescence of  $NV^-$  centers under laser excitation is brighter if the center is initially in  $m_S = 0$  and dimmer if it is in  $m_S = \pm 1$  states. This phenomenon allows optical read-out of the spin state by monitoring the photoluminescence rate. Additionally, the ground state with  $m_S = 0$  of the  $NV^-$  center can be prepared by continuous illumination that cycles  $NV^-$  centers through ground state—excited state—ground state transitions. Since the  $m_S = \pm 1$  state can transition to the  $m_S = 0$ , but no reverse transition is available, eventually, the center ends up in  $m_S = 0$  with high probability. In all, the spin-dependent optical relaxation allows the spin state to be both initialized and read out.

The spin state of the  $NV^-$  center can also be controlled with microwaves. When the microwave photon energy matches the energy difference between the ground levels with spin projection  $m_S = 0$  and the  $m_S = \pm 1$  spin state, transitions occur. The microwave energies at this resonance conditions are given by

$$E_{\text{MW}} = hf_{\text{MW}} = hD_{\text{GS}} + g\mu_B\Delta m_S B + m_I A_{\text{GS}}^{\text{HF}}, \quad (1)$$

where  $h \approx 6.62 \times 10^{-34}$  J/Hz is the Planck constant,  $f_{\text{MW}}$  is the microwave frequency,  $D_{\text{GS}} \approx 2.87$  GHz is the zero-field splitting,  $g \approx 2$  is the electron  $g$ -factor inside the diamond lattice,  $\mu_B \approx 9.27$  J·T<sup>-1</sup> is the Bohr magneton,  $m_S$  is the spin projection difference between the final and initial ground states,  $B$  is the applied magnetic field,  $m_I$  is the nuclear spin projection (preserved in the transition), and  $A_{\text{GS}}^{\text{HF}}$  is the energy correction due to the hyperfine interaction of the ground state levels with <sup>14</sup>N nucleus (spin  $I = 1$ ). Note that strain-induced splitting of the energy levels in diamond should also be considered when measuring small magnetic fields below 1 mT.

Optically detected magnetic resonance [47,48] is observed as a reduction in photoluminescence. Constant illumination populates the  $m_S = 0$  state, and dips in the photon count are observed when microwaves induce transitions to the  $m_S = \pm 1$  states. One can extract value of the external magnetic field  $B$  from the frequencies of the dips in the photoluminescence spectrum that correspond to the frequencies when  $NV^-$  center transitions to  $m_S = +1$  and  $m_S = -1$  states (Fig. 1(c)). This technique is a basis of  $NV^-$  magnetometry.

The resonance frequencies described in (1) yield a model for the normalized photon count signal ( $y = \{\mu\}$ ) that is a combination of three Lorentzian curves, one for each of the <sup>14</sup>N nuclear  $I_z$  states in the hyperfine interaction-split spectrum of the  $NV^-$  center:

$$\mu = 1 - \frac{a \cdot k_{\text{NP}}}{(f - f_B - \Delta f_{\text{HF}})^2 + \Omega^2} - \frac{a}{(f - f_B)^2 + \Omega^2} - \frac{a/k_{\text{NP}}}{(f - f_B + \Delta f_{\text{HF}})^2 + \Omega^2}. \quad (2)$$

Here  $f_B$  is the center resonance frequency that corresponds to the  $NV^-$  center transition from  $\{m_S = 0, m_I = 0\}$  to  $\{m_S = +1, m_I = 0\}$  state,  $\Delta f_{\text{HF}} = A_{\text{GS}}^{\text{HF}}/h$  is the hyperfine splitting,  $a$  is an overall contrast factor,  $\Omega$  is a linewidth, and  $k_{\text{NP}}$  characterizes the nuclear polarization. The coupling between  $NV^-$  center electrons and the nitrogen nucleus spin (naturally abundant

$^{14}\text{N}$ ,  $I=1$ ) leads to the weak spin transfer of constant polarization of the electron spin to nucleus. However, the nitrogen nucleus is not fully polarized in the presence of slight misalignment of the external magnetic field with the axis of the  $\text{NV}^-$  center [49,50]. This leads to the splitting of the  $\text{NV}^-$  center transitions into three photoluminescence dips of different amplitudes corresponding to  $m_J = -1, 0$  and  $+1$ , which are separated in frequency by the hyperfine splitting  $f_{\text{HF}}$  (Fig. 1(c)). For every measurement with microwave excitation, a reference photon count with microwaves switched off is used as a normalizing factor. Throughout this paper, we treat the excitation frequency  $f$  as the lone experimental setting design  $d = \{f\}$  and the five parameters  $\theta = \{f_B, f_{\text{HF}}, a, \Omega, k_{\text{NP}}\}$  as unknowns.

We use the triple-resonance spectrum described by (2) to compare the effectiveness of measurement protocols. The goal of the experiment is to determine the center resonance frequency  $f_B$ . The external magnetic field in  $\text{NV}^-$  magnetometry is given by the equation  $|B| = (h/g\mu_B) \cdot (f_B - D_{\text{GS}})$ , where  $g\mu_B/h \approx 28$  MHz/mT is the combination of the physical constants. The search range for the signal frequency was from 3040 MHz to 3200 MHz, which corresponds the magnetic field in the range from 6 mT to 12 mT. The generated electromagnet field was set to  $B \approx 8.32$  mT (picked by a random number generator) for the results shown in this paper, corresponding to the  $\text{NV}^-$  resonance frequency  $f_B \approx 3103$  MHz. The field was treated as an unknown in the measurements and data analysis.

In the conventional  $\text{NV}^-$  magnetometry measurements the photoluminescence of the sample was monitored while scanning the microwave frequency from 3040 MHz to 3200 MHz with 20 kHz step. Hence, each frequency scan consisted of 8000 normalized photoluminescence measurements.

The sequential Bayesian experiment design measurements iterated over a three-step cycle comprising a setting choice (design) from the allowed microwave frequencies, measurement, and data analysis via Bayesian inference. Here, we provide an overview of the process, and direct the interested reader to the Supplemental Material [44] (sections S.2 and S.3) and the references [27,34,51,52] for more detailed descriptions.

Bayesian methods treat the unknown parameters  $\theta$  as random variables with a probability distribution  $p(\theta)$ . In this application,  $\theta = \{f_B, f_{\text{HF}}, a, \Omega, k_{\text{NP}}\}$  are the parameters of the model function given in Eq. (2). After  $n$  iterations, the parameters are described by a conditional distribution  $p(\theta | \mathbf{y}_n, \mathbf{d}_n)$  given accumulated measurement results  $\mathbf{y}_n = (y_1, y_2, \dots, y_n)$  obtained at frequency settings (designs)  $\mathbf{d}_n = \{d_1, d_2, \dots, d_n\}$ .

In the  $n + 1^{\text{th}}$  iteration, the experiment design step uses the parameter distribution  $p(\theta | \mathbf{y}_n, \mathbf{d}_n)$ , to inform the choice of a setting design  $d_{n+1}$  for the next measurement. The algorithm models a distribution of measurement predictions for each possible design and then predicts the average improvement in the parameter distribution that would result from the predicted data. ‘‘Improvement’’ is quantified as a predicted change in the information entropy of the parameter distribution and it is expressed as a utility function  $U(d)$  [53,54]. The derivation of  $U(d)$  produces a qualitatively intuitive result: it does the most good to ‘‘pin down’’ the measurement results where they are sensitive to parameter variations. The new setting  $d_{n+1}$  is selected to maximize  $U(d)$ .

After the setting  $d_{n+1}$  is used to obtain the measurement result  $y_{n+1}$  these values are used to refine the parameter distribution. Using Bayesian inference,

$$p(\boldsymbol{\theta} | \mathbf{y}_{n+1}, \mathbf{d}_{n+1}) \propto p(y_{n+1} | \boldsymbol{\theta}, d_{n+1}) p(\boldsymbol{\theta} | \mathbf{y}_n, \mathbf{d}_n) \quad (3)$$

Where  $p(y_{n+1} | \boldsymbol{\theta}, d_{n+1})$  is the *likelihood*, the probability of observing the measured value  $y_{n+1}$  calculated for arbitrary parameter values  $\boldsymbol{\theta}$  given the frequency setting  $d_{n+1}$ . With increasing iteration number, the parameter distribution typically narrows, reflecting increasingly precise estimates of the parameter values.

In each iteration, the sequential Bayesian experiment design algorithm makes an informed setting decision and incorporates new data to inform the next decision. On a qualitative level, the Bayesian method formalizes an intuitive approach of making rough initial measurements to guide later runs, but the Bayesian method offers additional advantages. Bayesian inference incorporates new data, allowing for semicontinuous monitoring of “fitting” statistics, and result-based stopping criteria. The utility function provides a non-heuristic, flexible, data-based method for setting decisions. These advantages are especially important for situations where automation is required, speed is essential, or measurement data is expensive.

Software and documentation for sequential Bayesian experiment design is provided online [55].

## EXPERIMENTAL DETAILS

In this study, we used a commercially available single crystal diamond grown by chemical vapor deposition (CVD). Sample size was 3.0 mm × 3.0 mm × 0.3 mm, with {100} top surface orientation and surface roughness below 30 nm. The diamond (type IIa) had nitrogen concentration below 1 ppm and boron concentration below 0.05 ppm according to the manufacturer. The sample was mounted on top of the 50 mm long microstrip line, which was used to supply microwaves to manipulate spin state of the NV<sup>-</sup> center. The microstrip line with the sample was placed in an electromagnet between pincer-shaped poles that were oriented to align with the [111] direction of the diamond lattice ( $\arcsin\sqrt{2/3} \approx 54.7^\circ$  from the vertical). In this arrangement, the magnetic field is pointing along one of the four possible orientations of NV<sup>-</sup> center axes (vector connecting nitrogen atom to the vacancy site).

A green laser with 520 nm wavelength was used to optically excite NV<sup>-</sup> center. The 0.7 numerical aperture (NA) objective of a custom-built confocal microscope was located above the sample to focus laser excitation inside the diamond and to collect fluorescence from the NV<sup>-</sup> center. A dichroic beamsplitter with the edge at 650 nm was used to separate excitation laser light from the collected fluorescence. After further wavelength selection with 647 nm long-pass filters, the collected fluorescence was coupled into a multimode fiber and directed to the photon detector. For each data point, a 50 ms photon count with the microwaves on was divided by a subsequent 50 ms reference count with microwaves off. The excitation using green laser light was on continuously. Only 10 mW of microwave power (at the source) and 225 μW of laser power (before the objective) were sent to the sample. The laser power was set using the linear polarizer and the half-wave plate. The combination of laser

power, microwave power and counting time produced measurements with a signal-to-noise ratio on the order of 1. Such experimental setup showcases ability of sequential Bayesian experiment design to locate and measure complex multiple-peak signal even in extremely noisy data, and shows its broad dynamical range for sensitivity.

## RESULTS AND DISCUSSION

First, we report the results of the conventional  $NV^-$  magnetometry measurements. Figure 1(d) shows the photoluminescence data measured in one frequency scan. Dips in the photoluminescence spectrum corresponding to optically detected magnetic resonance are visible with a signal-to-noise ratio on the order of one. We follow the conventional approach to improve the signal-to-noise, which is to remeasure the same scanning range and average the data in the scans. Figures 1(e) – 1(g) show averaged data for increasing numbers of scans. The signal-to-noise ratio improves as the inverse square root of the number of the averaged scans.

To gauge the evolution of parameter uncertainty as a function of scan number, we “fit” the averaged data using Bayesian inference to determine mean values and standard deviations from the parameter distribution. To allow direct comparison, we used the same algorithm for Bayesian inference as in the sequential design data below. Like the overall signal-to-noise ratio, the standard deviation of the resonance frequency also follows an inverse square root dependence on the total number of the scans (Fig. 1(h)).

Photoluminescence data of the  $NV^-$  magnetometry measurements using sequential Bayesian experiment design are shown in Figs. 1(i) – 1(l). Here the data are plotted without averaging. While initial frequency sampling roams across the whole allowed frequency range (Figs. 1(i) and 1(j)), the later measurements almost exclusively focus on the signal location near the resonance dips where the photoluminescence value is lower (Figs. 1(k) and 1(l)). The standard deviation  $\sigma_f$  of the center resonance frequency  $f_B$  is plotted as a function of the number of measurements in Fig. 1(m). The standard deviation drops by three orders of magnitude within the first two hundred measurements.

We plot evolution of the probability distribution  $p(\theta)$  of the signal frequency  $f_B$  and hyperfine splitting  $f_{HF}$  parameters in Figure 2. The probability distribution is implemented using sequential Monte Carlo where the probability density in parameter space is represented by the density of points and by a weight factor attached to each point. After each measurement, the weights are recalculated using Bayesian inference. Fig. 2(a) shows the initial, *prior* distribution, which consists of 10 000 points distributed through the parameter space with equal weights of  $10^{-4}$  (Fig. 2(a)). The sum of all weights is normalized to 1.

Fig. 2(b) plots the probability distribution after the first measurement, which yielded  $\mu_1 = 1.014$  for the normalized photon count at  $f_1 = 3154.26$  MHz. Since the resonances are dips in the photon count, values of  $\mu > 1$  reduce the likelihood that the resonances are located near the measurement frequency  $f_1$ . To highlight this effect, distribution points with weights  $w < 10^{-4}$  are colored cyan and weights  $w = 10^{-4}$  are red. After several cycles of measurements and updating the weights, a resampling algorithm redistributes points, allowing high-weight

points to survive, multiply, and diffuse slightly while low-weight points face a greater probability of elimination (see section S.4 of Supplemental Material). Resampling allows the computational resources to be focused on high-probability regions of parameter space without completely abandoning low-probability regions. The effects of resampling are visible in Fig. 2(d) and later panels with the higher concentration of points near 3090 MHz. After the first two hundred measurements, the  $p(f_B)$  distribution has effectively contracted from spanning over the range of 150 MHz to less than 1 MHz (Figs. 2(k) and 2(l)). Interestingly, redistribution of the weights also allows probability distribution to diffuse beyond the initial boundary conditions. For example, initial weights occupy  $f_{\text{HF}}$  parameter space from 1 MHz to 3 MHz (Figs. 2(a) – 2(c)), but after 100 measurements, resampling steps have allowed the probability distribution to span  $f_{\text{HF}}$  parameter space from 0.5 MHz to 4 MHz. This diffusion allows slow convergence to values outside the prior distribution—i.e., in the areas where the experimenter does not expect to find final parameters' values—which is helpful in cases when experimenter does not have an accurate initial estimate for parameter.

The evolution of the  $\text{NV}^-$  magnetometry measurements using sequential Bayesian experiment design is in sharp contrast with the evolution of the conventional  $\text{NV}^-$  magnetometry measurements. The standard deviation of the signal frequency using sequential Bayesian experiment design follows a typical pattern displayed in Figure 1(m). After an initial period of broad sampling of parameter space, the algorithm focuses measurements near the resonance frequencies (Fig. 3(a)) and the probability distribution  $p(f_B)$  contracts rapidly. After this contraction, the standard deviation of  $f_B$  decreases as the inverse square root of the total number of the measurements  $n$  (Fig. 1(m)). In contrast, the standard deviation of the signal frequency in the swept-frequency measurements does not go through such rapid contraction phase and follows an inverse square root of  $n$  scaling from the beginning (Fig. 1(h)).

The difference in the measurement strategies can be clearly seen in the photoluminescence data for the first thousand measurements. Sequential Bayesian experiment design has already narrowed down the probability distribution  $p(f_B)$  for the signal frequency, and most of the measurements are taken at the signal position—the location of the three hyperfine-split dips (Figs. 3(a) orange solid circles, 3(c) and 3(d)). In contrast, the frequency sweep in the conventional measurements has not even reached the frequency where the signal is located, and all 1000 data points were spent on measuring the background (Figs. 3(a) purple solid circles and 3(b)). After 24000 measurements (3 full range conventional sweep scans), only 3 measurements were performed at each frequency at the signal location by the conventional  $\text{NV}^-$  magnetometry (Fig. 3(g)), compared with peak of 214 measurements per frequency for sequential Bayesian experiment design measurements (Fig. 3(j)). This concentration of measurements results in a standard deviation of the averaged Bayesian measurement (Fig 3(i) that is an order of magnitude smaller than in the conventional measurement (Fig. 3(f)).

An interesting behavior of the utility function  $U(d=\{f\})$  can be seen in Fig. 3(j). In the central,  $m_I=0$  photoluminescence dip area most of the measurements are concentrated near its center (frequency  $f_B$ ) while at the outer dips located at  $f_B - f_{\text{HF}}$  and  $f_B + f_{\text{HF}}$ ,

measurements are concentrated on the sides of the dips, producing double-peak structures in the distribution of the measurements (Fig. 3(j)). In simulations and measurements on single-dip resonances, similar focus on the sides of dips is typical behavior, and it is consistent with the high sensitivity of the sides of the dip model to the resonance frequency parameter. On the other hand, the central concentration of measurements that we observe at the central dip in Fig. 3(j) would be atypical behavior for single resonances. We speculate that this behavior stems from the triple-resonance model's (2) implicit assumption that the center resonance lies at the midpoint between the outer resonances.

The “smart” measurement strategy of taking data into account on the fly—instead of waiting until the end of the experiment—allows the  $NV^-$  magnetometry based on sequential Bayesian experiment design to dramatically outperform conventional  $NV^-$  magnetometry. For example, to achieve the precision of  $\sigma_f = 5.5 \cdot 10^{-3}$  MHz standard deviation of the signal frequency, the conventional sweep-based  $NV^-$  magnetometry requires  $10^6$  measurements, while the  $NV^-$  magnetometry based on sequential Bayesian experiment design requires only 24 350 measurements to achieve the same precision. Using the ratio between  $1/\sqrt{n}$  scaling of the standard deviations of the signal frequencies for two methods (Fig. 4), sequential Bayesian experiment design magnetometry was determined to be 45 times faster than the conventional measurement approach.

Up to this point, we have compared measurement protocols on the basis of the number of measurements, but “wall-clock” time may be a more relevant basis for comparison, since sequential Bayesian experiment design comes with an added cost of computational time. Photons from  $NV^-$  centers are counted for 100 ms at each data point (50 ms with microwaves on, followed by 50 ms with microwaves off). In the conventional protocol, the average time spent on measuring one data point is 150 ms. The additional 50 ms time is spent on communication between the devices, saving data etc. Using sequential Bayesian experiment design, the average time spent on measuring one data point is 204 ms, a 36 % (54 ms) increase in measurement time compared with the conventional setup. The additional time represents the added computational cost of Bayesian inference and utility calculations for each measurement. The computation time depends on computer hardware and programming methods. Here we report results using a single processor core of an ordinary PC programmed in Python using the Numpy package (see S.4 of Supplemental Material). Compiled code and parallel computation offer avenues for significant reductions in computation time [56,57]. The cost of an additional processor (several hundred dollars) is also negligible compared with the cost of the other hardware typically used in the  $NV^-$  magnetometry experiments. However, in the light of the 4400 % speedup, the associated additional Bayesian computation time (36 % longer measurement time) is negligible, even when performed on the ordinary processor and without using parallel threads.

In the  $NV^-$  measurements that we have carried out using sequential Bayesian experiment design, we always observe more than one order of magnitude speedup. The amount of speedup depends on experimental setup, signal, set of parameters and settings, and reaches close to two orders of magnitude for some of the experiments that we have carried out. A big factor that influences the speedup is the fraction of settings space occupied by the signal, compared to the whole space spanned by the settings  $d$  (scanning or sensing range). In the



experiment described in this paper, signal occupies roughly 10 % of the whole scanning range (16 MHz out of the 160 MHz frequency range: 8 MHz is occupied by the dips and 4 MHz on each side by their shoulders). This value can be much smaller in magnetometers/sensors with broad sensing range, which will lead to even larger speedups. However, a focus on the measurements with maximum utility function allows sequential Bayesian experiment design to be beneficial even for measurements where signal is present throughout the whole settings space  $d$  (see section S.5 of the Supplemental Material for more details). As a rule of thumb, the more time an experimental procedure spends on measuring data with low utility function values (for example, areas away from the signal or areas with small signal-to-noise ratio), the more beneficial will be implementation of the measurements using sequential Bayesian experiment design. Sequential Bayesian experiment design can be particularly useful for maturing NV<sup>-</sup> center magnetometry technology and moving it into the market. Scanning magnetometers or compact in-the-field sensors need to obtain data as fast as possible. Sequential Bayesian experiment design can be used as a much faster alternative to the numerous averaging scans. It can also be combined with other approaches that improve sensitivity, such as magnetometry using complicated pulse sequences. While the current study focused on NV<sup>-</sup> center magnetometry using sequential Bayesian experiment design, the reported methods—and corresponding speedups—are directly transferable into other areas beyond NV<sup>-</sup> centers magnetometry.

## CONCLUSION

In this study, we report more than order-of-magnitude speedup of NV<sup>-</sup> magnetometry using sequential Bayesian experimental design, compared with the conventional NV<sup>-</sup> magnetometry. The large gain in the speed/precision of the NV<sup>-</sup> center magnetometry using sequential Bayesian experiment design demonstrated in this study is readily translatable to other applications beyond magnetometry and experiments with the NV<sup>-</sup> centers. The developed `optbayesxpt` software that was used to carry out sequential Bayesian experiment design measurements is available online for public use free of charge.

## Supplementary Material

Refer to Web version on PubMed Central for supplementary material.

## ACKNOWLEDGEMENTS

S.D. and K.A. acknowledge support under the Cooperative Research Agreement between the University of Maryland and the National Institute of Standards and Technology Physical Measurement Laboratory, Award 70NANB14H209, through the University of Maryland. The authors thank Adam Pintar for many helpful discussions.

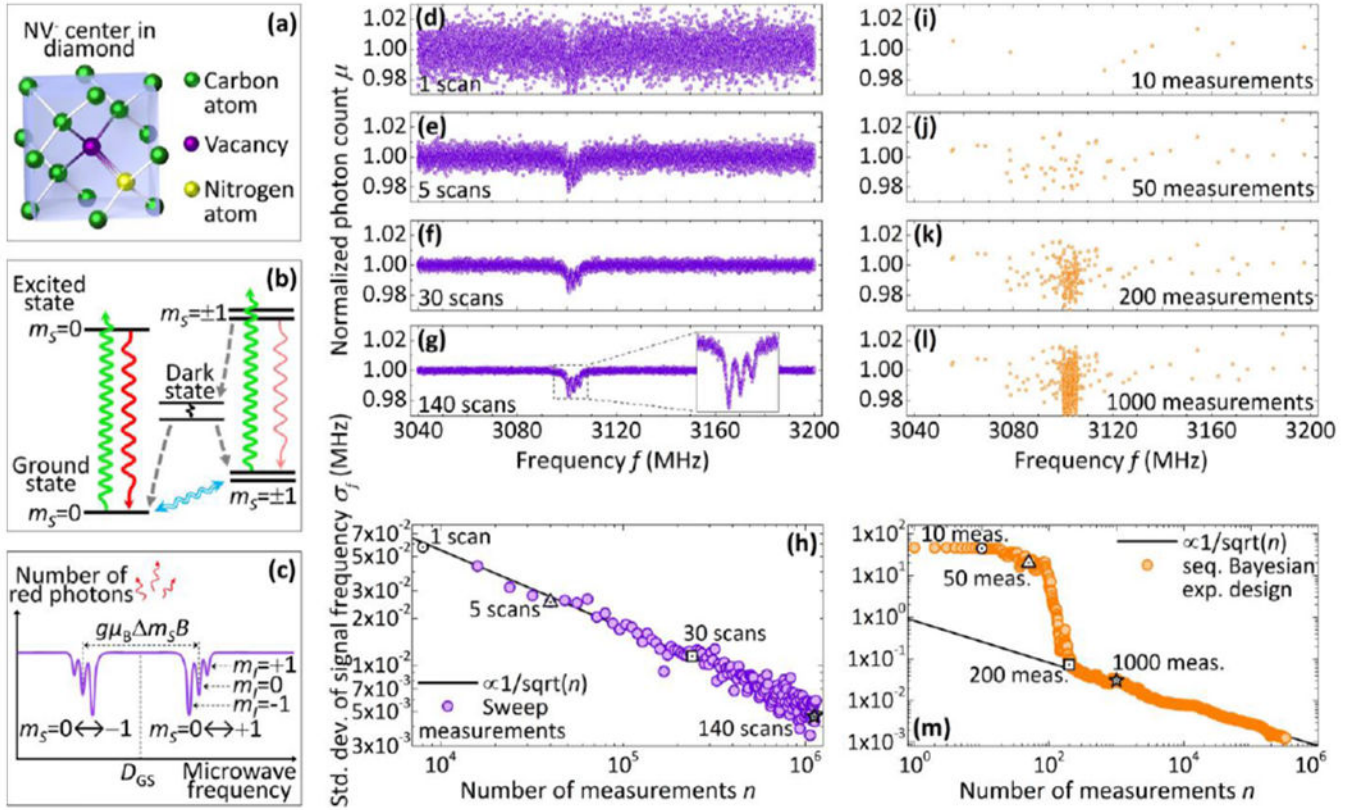
## REFERENCES

- [1]. Wu Y, Wang Y, Qin X, Rong X, and Du J, A programmable two-qubit solid-state quantum processor under ambient conditions, *NPJ Quantum Inf.* 5, 9 (2019).
- [2]. Beveratos A, Brouri R, Gacoin T, Villing A, Poizat J-P, and Grangier P, Single photon quantum cryptography, *Phys. Rev. Lett* 89, 187901 (2002). [PubMed: 12398636]
- [3]. Fuchs GD, Burkard G, Klimov PV, and Awschalom DD, A quantum memory intrinsic to single nitrogen—vacancy centres in diamond, *Nat. Phys* 7, 789 (2011).

- [4]. Yang WL, Yin ZQ, Hu Y, Feng M, and Du JF, High-fidelity quantum memory using nitrogen-vacancy center ensemble for hybrid quantum computation, *Phys. Rev. A* 84, 010301 (2011).
- [5]. Vijayanthimala V and Chang H-C, Functionalized fluorescent nanodiamonds for biomedical applications, *Nanomedicine* 4, 47 (2009). [PubMed: 19093895]
- [6]. Badea I and Kaur R, Nanodiamonds as novel nanomaterials for biomedical applications: drug delivery and imaging systems, *Int. J. Nanomedicine* 8, 203 (2013). [PubMed: 23326195]
- [7]. Kolkowitz S, Bleszynski Jayich AC, Unterreithmeier QP, Bennett SD, Rabl P, Harris JGE, and Lukin MD, Coherent sensing of a mechanical resonator with a single-spin qubit, *Science* 335, 1603 (2012). [PubMed: 22362881]
- [8]. Kucsko G, Maurer PC, Yao NY, Kubo M, Noh HJ, Lo PK, Park H, and Lukin MD, Nanometre-scale thermometry in a living cell, *Nature* 500, 54 (2013). [PubMed: 23903748]
- [9]. Neumann P, Jakobi I, Dolde F, Burk C, Reuter R, Waldherr G, Honert J, Wolf T, Brunner A, Shim JH, Suter D, Sumiya H, Isoya J, and Wrachtrup J, High-precision nanoscale temperature sensing using single defects in diamond, *Nano Lett.* 13, 2738 (2013). [PubMed: 23721106]
- [10]. Dolde F, Fedder H, Doherty MW, Nöbauer T, Rempff F, Balasubramanian G, Wolf T, Reinhard F, Hollenberg LCL, Jelezko F, and Wrachtrup J, Electric-field sensing using single diamond spins, *Nat. Phys* 7, 459 (2011).
- [11]. Balasubramanian G, Chan IY, Kolesov R, Al-Hmoud M, Tisler J, Shin C, Kim C, Wojcik A, Hemmer PR, Krueger A, Hanke T, Leitstorfer A, Bratschitsch R, Jelezko F, and Wrachtrup J, Nanoscale imaging magnetometry with diamond spins under ambient conditions, *Nature* 455, 648 (2008). [PubMed: 18833276]
- [12]. Maze JR, Stanwix PL, Hodges JS, Hong S, Taylor JM, Cappellaro P, Jiang L, Dutt MVG, Togan E, Zibrov AS, Yacoby A, Walsworth RL, and Lukin MD, Nanoscale magnetic sensing with an individual electronic spin in diamond, *Nature* 455, 644 (2008). [PubMed: 18833275]
- [13]. Du C, van der Sar T, Zhou TX, Upadhyaya P, Casola F, Zhang H, Onbasli MC, Ross CA, Walsworth RL, Tserkovnyak Y, and Yacoby A, Control and local measurement of the spin chemical potential in a magnetic insulator, *Science* 357, 195 (2017). [PubMed: 28706070]
- [14]. Taylor JM, Cappellaro P, Childress L, Jiang L, Budker D, Hemmer PR, Yacoby A, Walsworth R, and Lukin MD, High-sensitivity diamond magnetometer with nanoscale resolution, *Nat. Phys* 4, 810 (2008).
- [15]. Rondin L, Tetienne J-P, Hingant T, Roch J-F, Maletinsky P, and Jacques V, Magnetometry with nitrogen-vacancy defects in diamond, *Reports Prog. Phys* 77, 056503 (2014).
- [16]. Maletinsky P, Hong S, Grinolds MS, Hausmann B, Lukin MD, Walsworth RL, Loncar M, and Yacoby A, A robust scanning diamond sensor for nanoscale imaging with single nitrogen-vacancy centres, *Nat. Nanotechnol* 7, 320 (2012). [PubMed: 22504708]
- [17]. Reith P and Hilgenkamp H, Analysing magnetism using scanning squid microscopy, *Rev. Sci. Instrum* 88, 123706 (2017). [PubMed: 29289200]
- [18]. Degen CL, Reinhard F, and Cappellaro P, Quantum sensing, *Rev. Mod. Phys* 89, 035002 (2017).
- [19]. Mitchell MW and Palacios Alvarez S, Colloquium : quantum limits to the energy resolution of magnetic field sensors, *Rev. Mod. Phys* 92, 021001 (2020).
- [20]. Schloss JM, Barry JF, Turner MJ, and Walsworth RL, Simultaneous broadband vector magnetometry using solid-state spins, *Phys. Rev. Appl* 10, 034044 (2018).
- [21]. Balasubramanian P, Osterkamp C, Chen Y, Chen X, Teraji T, Wu E, Naydenov B, and Jelezko F, Dc magnetometry with engineered nitrogen-vacancy spin ensembles in diamond, *Nano Lett.* 19, 6681 (2019). [PubMed: 31430171]
- [22]. Shin CS, Avalos CE, Butler MC, Trease DR, Seltzer SJ, Peter Mustonen J, Kennedy DJ, Acosta VM, Budker D, Pines A, and Bajaj VS, Room-temperature operation of a radiofrequency diamond magnetometer near the shot-noise limit, *J. Appl. Phys* 112, 124519 (2012).
- [23]. El-Ella HAR, Ahmadi S, Wojciechowski AM, Huck A, and Andersen UL, Optimised frequency modulation for continuous-wave optical magnetic resonance sensing using nitrogen-vacancy ensembles, *Opt. Express* 25, 14809 (2017). [PubMed: 28789064]
- [24]. Clevenson H, Pham LM, Teale C, Johnson K, Englund D, and Braje D, Robust high-dynamic-range vector magnetometry with nitrogen-vacancy centers in diamond, *Appl. Phys. Lett* 112, 252406 (2018).

- [25]. Ambal K and McMichael RD, A differential rate meter for real-time peak tracking in optically detected magnetic resonance at low photon count rates, *Rev. Sci. Instrum* 90, 023907 (2019). [PubMed: 30831689]
- [26]. Liu G, Chen M, Liu Y-X, Layden D, and Cappellaro P, Repetitive readout enhanced by machine learning, *Mach. Learn. Sci. Technol* 1, 015003 (2020).
- [27]. Chaloner K and Verdinelli I, Bayesian experimental design: a review, *Stat. Sci* 10, 273 (1995).
- [28]. Bayes T, An essay towards solving a problem in the doctrine of chances, *Philos. Trans. R. Soc. London* 53, 370 (1763).
- [29]. Laplace PS, Memoire sur la probabilite des causes par les evenemens, *Mem. Math. Phys* 6, 621 (1774).
- [30]. Laplace PS, Memoir on the probability of the causes of events, *Stat. Sci* 1, 364 (1986).
- [31]. Jaynes ET, *Probability Theory* (Cambridge University Press, 2003).
- [32]. Mabuchi H, Dynamical identification of open quantum systems, *Quantum Semiclassical Opt. J. Eur. Opt. Soc. Part B* 8, 1103 (1996).
- [33]. Gambetta J and Wiseman HM, State and dynamical parameter estimation for open quantum systems, *Phys. Rev. A* 64, 042105 (2001).
- [34]. Granade CE, Feme C, Wiebe N, and Cory DG, Robust online hamiltonian learning, *New J. Phys* 14, 103013 (2012).
- [35]. Gammelmark S and Mølmer K, Bayesian parameter inference from continuously monitored quantum systems, *Phys. Rev. A* 87, 032115 (2013).
- [36]. Scerri E, Gauger EM, and Bonato C, Extending qubit coherence by adaptive quantum environment learning, *New J. Phys* 22, (2020).
- [37]. Negretti A and Mølmer K, Estimation of classical parameters via continuous probing of complementary quantum observables, *New J. Phys* 15, (2013).
- [38]. Dinani HT, Berry DW, Gonzalez R, Maze JR, and Bonato C, Bayesian estimation for quantum sensing in the absence of single-shot detection, *Phys. Rev. B* 99, 125413 (2019).
- [39]. Schwartz I, Roskopf J, Schmitt S, Tratzmiller B, Chen Q, McGuinness LP, Jelezko F, and Plenio MB, Blueprint for nanoscale nmr, *Sci. Rep* 9, 6938 (2019). [PubMed: 31061430]
- [40]. Bonato C and Berry DW, Adaptive tracking of a time-varying field with a quantum sensor, *Phys. Rev. A* 95, 1 (2017).
- [41]. Wang J, Paesani S, Santagati R, Knauer S, Gentile AA, Wiebe N, Petruzzella M, O'brien JL, Rarity JG, Laing A, and Thompson MG, Experimental quantum hamiltonian learning, *Nat. Phys* 13, 551 (2017).
- [42]. Bonato C, Blok MS, Dinani HT, Berry DW, Markham ML, Twitchen DJ, and Flanson R, Optimized quantum sensing with a single electron spin using real-time adaptive measurements, *Nat. Nanotechnol* 11, 247 (2016). [PubMed: 26571007]
- [43]. Santagati R, Gentile AA, Knauer S, Schmitt S, Paesani S, Granade C, Wiebe N, Osterkamp C, McGuinness LP, Wang J, Thompson MG, Rarity JG, Jelezko F, and Laing A, Magnetic-field learning using a single electronic spin in diamond with one-photon readout at room temperature, *Phys. Rev. X* 9, 021019 (2019).
- [44]. See Supplemental Material at <http://link.aps.org/supplemental/10.1103/PhysRevApplied.14.054036> for additional details and discussion on structure and physics of NV<sup>-</sup> center, sequential Bayesian experiment design, implementation of probability distributions, specifications of the computational hardware used for sequential Bayesian experiment design and speedup of the sequential Bayesian experiment design.
- [45]. Gruber A, Drabenstedt A, Tietz C, Fleury L, Wrachtrup J, and von Borczyskowski C, Scanning confocal optical microscopy and magnetic resonance on single defect centers, *Science* 276, 2012 (1997).
- [46]. Davies G and Hamer MF, Optical studies of the 1.945 eV vibronic band in diamond, *Proc. R. Soc. London. A. Math. Phys. Sci* 348, 285 (1976).
- [47]. Kohler J, Disselhorst JAJM, Donckers MCJM, Groenen EJJ, Schmidt J, and Moerner WE, Magnetic resonance of a single molecular spin, *Nature* 363, 242 (1993).

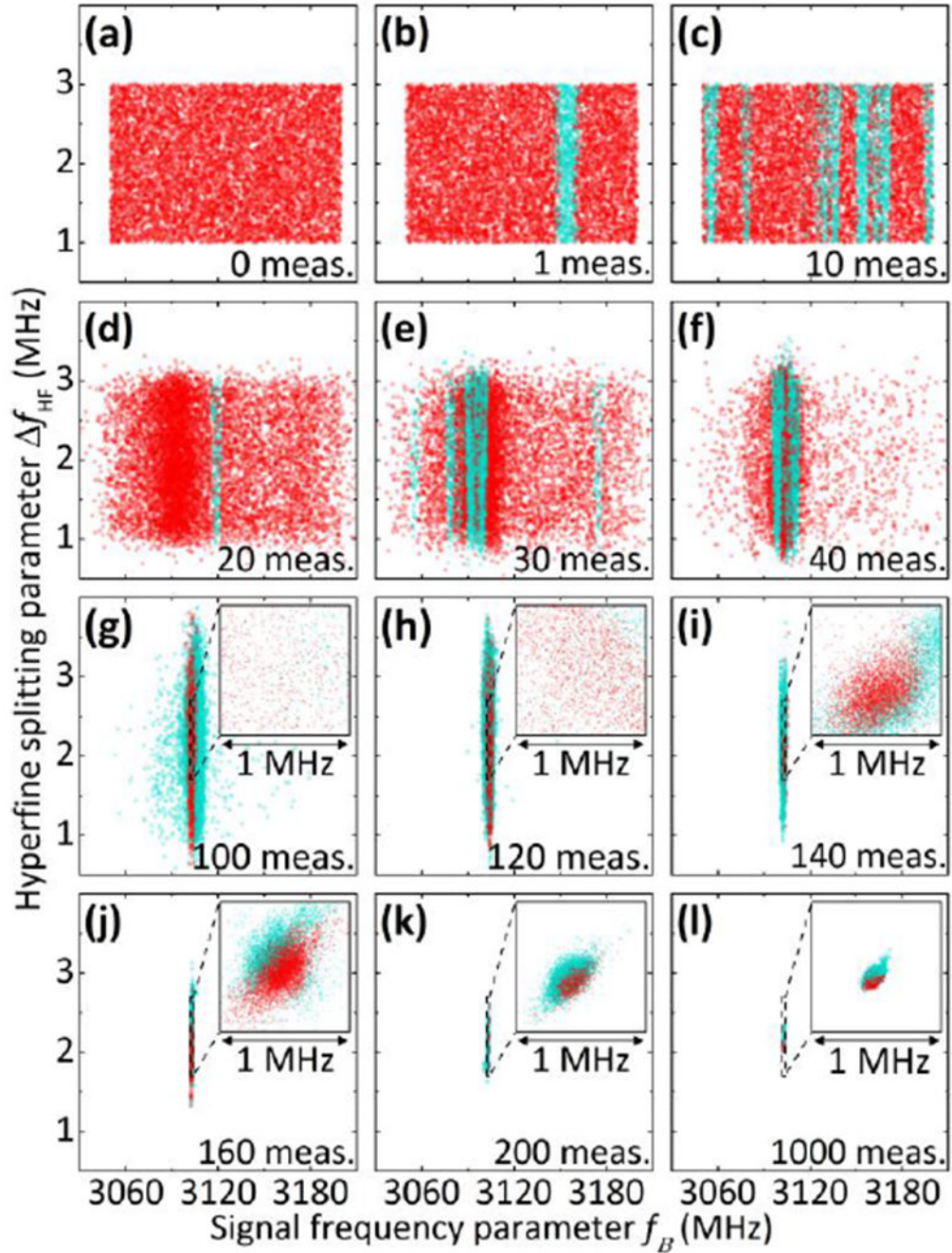
- [48]. Wrachtrup J, von Borczyskowski C, Bernard J, Orrit M, and Brown R, Optical detection of magnetic resonance in a single molecule, *Nature* 363, 244 (1993).
- [49]. Jacques V, Neumann P, Beck J, Markham M, Twitchen D, Meijer J, Kaiser F, Balasubramanian G, Jelezko F, and Wrachtrup J, Dynamic polarization of single nuclear spins by optical pumping of nitrogen-vacancy color centers in diamond at room temperature, *Phys. Rev. Lett* 102, 057403 (2009). [PubMed: 19257552]
- [50]. Fischer R, Jarmola A, Kehayias P, and Budker D, Optical polarization of nuclear ensembles in diamond, *Phys. Rev. B* 87, 125207 (2013).
- [51]. Lindley DV, On a measure of the information provided by an experiment, *Ann. Math. Stat* 27, 986 (1956).
- [52]. Huan X and Marzouk YM, Simulation-based optimal Bayesian experimental design for nonlinear systems, *J. Comput. Phys* 232, 288 (2013).
- [53]. Kullback S and Leibler RA, On information and sufficiency, *Ann. Math. Stat* 22, 79 (1951).
- [54]. Kullback S, *Information Theory and Statistics* (Dover Publications, 1968).
- [55]. McMichael RD, Optimal Bayesian Experiment Design Software [Online] (2020). <https://github.com/usnistgov/optbayesexpt>, McMichael RD, Optimal Bayesian Experiment Design Documentation [Online] (2020). <https://pages.nist.gov/optbayesexpt>
- [56]. Ryan EG, Drovandi CC, McGree JM, and Pettitt AN, A review of modern computational algorithms for Bayesian optimal design, *Int. Stat. Rev* 84, 128 (2016).
- [57]. Nicely MA and Wells BE, Improved parallel resampling methods for particle filtering, *IEEE Access* 7, 47593 (2019).



**FIG. 1.**

(a) Crystal structure of the  $\text{NV}^-$  center inside diamond lattice. Green spheres denote carbon atoms, yellow sphere is a nitrogen atom, purple sphere is a vacancy. Each white line corresponds to an  $\text{sp}^3$  bond created by a pair of electrons. (b) Schematic structure of the transitions between energy levels of the  $\text{NV}^-$  center.  $\text{NV}^-$  center in the ground state can be excited by the laser light (green arrows—transitions due to the absorbed photons); the process preserves spin projection  $m_S$ . From the excited state  $\text{NV}^-$  center can relax back to the ground state by emitting red photon ( $m_S = \pm 1$  or  $m_S = 0$  excited states; red arrow—transitions due to the emitted photons), or non-radiatively relax through the dark state (only  $m_S = \pm 1$  excited states; dashed gray arrow). Transition between the states with  $m_S = \pm 1$  and  $m_S = 0$  can be induced by microwaves (blue arrow). (c) Schematics of the photoluminescence spectrum of the  $\text{NV}^-$  center under application of microwave irradiation and the external magnetic field  $B$ . The six dips are present due to the Zeeman splitting and hyperfine interaction, (d) – (g) panels show the averaged data from (d) 1 scan, (e) 5 scans, (f) 30 scans, (g) 140 scans (inset shows enlarged signal area) of the conventional  $\text{NV}^-$  magnetometry using photoluminescence detection under sweeping of the microwave frequency. Magnetic field is calculated using the position of the signal (central dip) in the photoluminescence spectrum. (h) Dependence of the standard deviation of the signal frequency  $f_B$  on the number of photoluminescence measurements. Each solid purple circle corresponds to a unique number of averaged frequency sweep scans; each scan consists of 8000 measured data points. Black symbols correspond to the data from panels (d) – (g). Black solid line shows inverse square root scaling. Note the logarithmic scale. (i) – (l) panels

show the data from (i) 10, (j) 50, (k) 200, (l) 1000 photoluminescence measurements of the  $NV^-$  magnetometry using sequential Bayesian experiment design. (m) Dependence of the standard deviation of the signal frequency on the number of photoluminescence measurements. Each solid orange circle corresponds to a unique number of photoluminescence measurements. Black symbols correspond to the data from panels (i) – (l). Black solid line shows inverse square root scaling. Note the logarithmic scale.

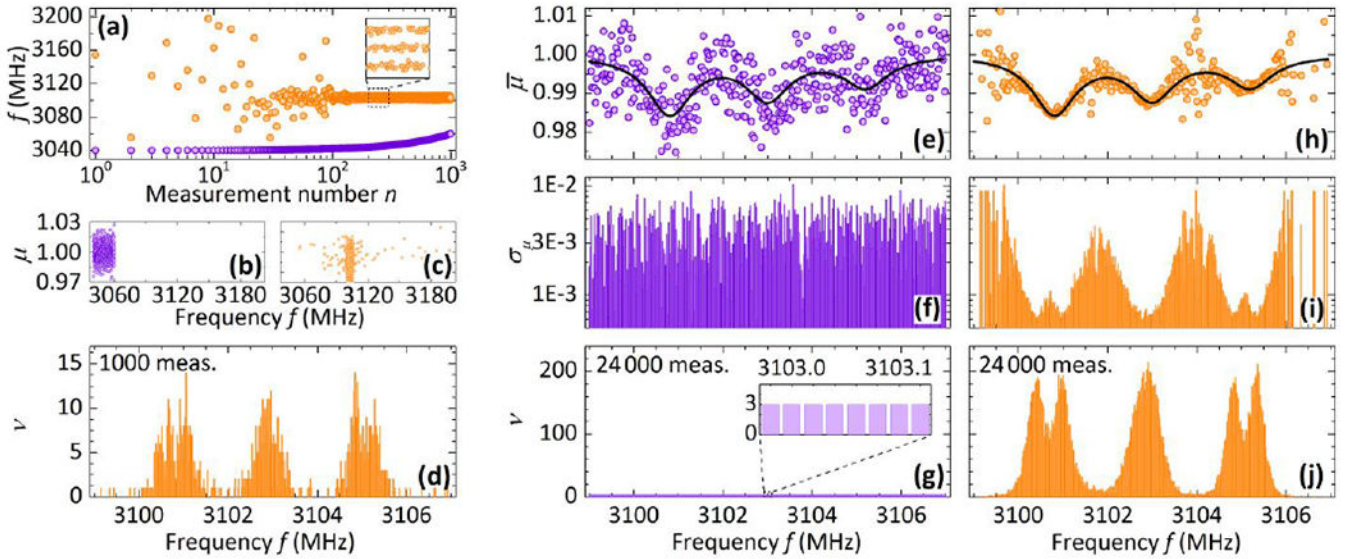


**FIG. 2.**

Dependence of the probability distributions for signal frequency and hyperfine splitting parameters on the number of the measurements in  $\text{NV}^-$  magnetometry using sequential Bayesian experiment design. Panels shows probability distributions after (a) 0, (b) 1, (c) 10, (d) 20, (e) 30, (f) 40, (g) 100, (h) 120, (i) 140, (j) 160, (k) 200, (l) 1000 measurements. Each probability distribution consists of 10 000 points in parameter space with weights adding up to 1. Color represents weight:  $< 10^{-4}$ —cyan,  $10^{-4}$ —red. Insets show zoomed-in area of

the probability distributions. All insets have the same size ( $1 \text{ MHz} \times 1 \text{ MHz}$ ), and span the same parameter space [(3102.5 MHz, 3103.5 MHz); (1.7 MHz, 2.7 MHz)].



**FIG. 3.**

(a) Dependence of the measurement frequency on the measurement number for the conventional  $\text{NV}^-$  magnetometry microwave frequency sweep scan (purple solid circles) and the  $\text{NV}^-$  magnetometry using sequential Bayesian experiment design (orange solid circles). Inset shows zoomed-in view of the area enclosed by the dashed rectangle. Photoluminescence data for the first 1000 measurements of (b) the conventional  $\text{NV}^-$  magnetometry microwave frequency sweep scan, and (c)  $\text{NV}^-$  magnetometry using sequential Bayesian experiment design. (d) Distribution of the measurement frequency for the first 1000 measurements of the  $\text{NV}^-$  magnetometry using sequential Bayesian experiment design, (e, h) Average normalized photon count  $\bar{\mu}$ , (f, i) standard deviation of the normalized photon count  $\sigma_{\mu}$  and (g, j) number of measurements  $\nu(f)$  dependence on the measurement frequency for the first 24 000 measurements. (e, f, g) correspond to data from the conventional  $\text{NV}^-$  magnetometry scan (purple); (h, i, j) correspond to data from the  $\text{NV}^-$  magnetometry using sequential Bayesian experiment design (orange). Black solid line (panels (e, h)) shows fitting using function  $\mu$  of *all* the measured data: 140 scans (1 120 000 measurements) of the conventional  $\text{NV}^-$  magnetometry and 330 000 measurements of the  $\text{NV}^-$  magnetometry using sequential Bayesian experiment design. Inset in panel (g) provides a zoomed-in view of the data.

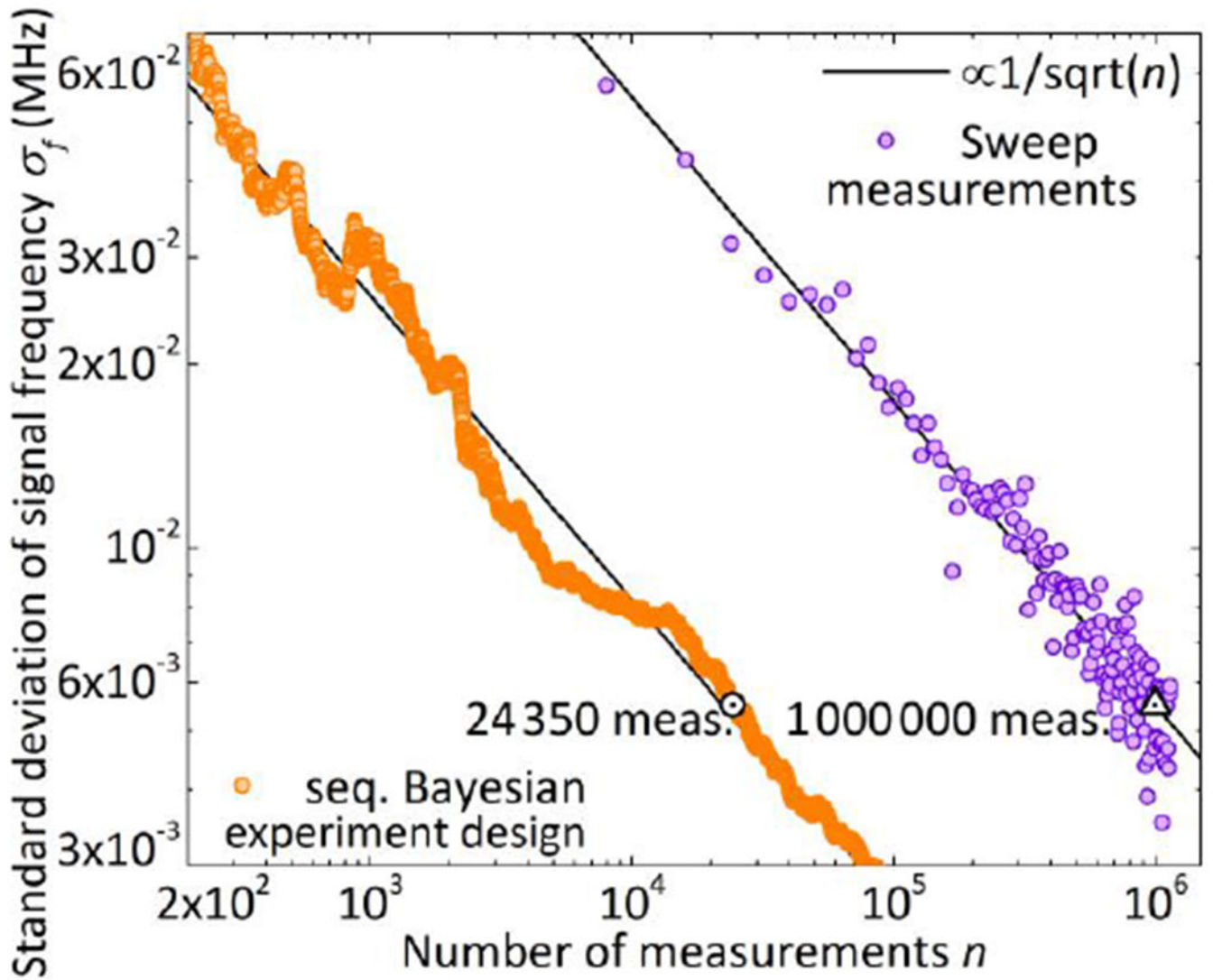


FIG. 4.

Dependence of the standard deviation of the signal frequency on the number of photoluminescence measurements. Each orange filled circle corresponds to a unique number of photoluminescence measurements using sequential Bayesian experiment design. Each purple filled circle corresponds to a unique number of averaged frequency sweep scans; each scan consists of 8000 measured photoluminescence data points. Black symbols correspond to equal standard deviation of the signal frequency for sequential Bayesian experiment design (black circle) and conventional sweep measurement (black triangle). Black solid lines show inverse square root scaling. Note the logarithmic scale.